Detection of vortical structures in sparse Lagrangian data using coherent-structure colouring

Martins, F. A.C.; Sciacchitano, A.; Rival, D. E.

Important note
To cite this publication, please use the final published version (if applicable).
Please check the document version above.

Detection of vortical structures in sparse Lagrangian data using coherent-structure colouring

F. A. C. Martins[1] · A. Sciacchitano[2] · D. E. Rival[1]

Abstract

In this study, vortical structures are detected on sparse Shake-The-Box data sets using the Coherent-Structure Colouring (CSC) algorithm. The performance of this Lagrangian approach is assessed by comparing the CSC-coloured tracks with the baseline vorticity field. The ability to extract vortical structures from sparse data is accessed on two Lagrangian particle tracking data sets: the flow past an Ahmed body and a swirling jet flow. The effects of two normalized parameters on the identification of vortical structures were defined and studied: the mean track length and the mean inter-particle distance. The accuracy of the vortical-structure detection problem through CSC is shown to improve with decreasing inter-particle distance values, whereas little dependence on the mean track length is observed at all. Overall, the CSC algorithm showed to yield accurate detection of coherent structures for inter-particle distances smaller than 15% of the characteristic dimension of the structure. However, the results quickly deteriorate for sparser Lagrangian data.

✉ D. E. Rival
   d.e.rival@queensu.ca

1   Department of Mechanical and Materials Engineering,
    Queen's University, Kingston, ON, Canada

2   Department of Aerodynamics, Faculty of Aerospace
    Engineering, Delft University of Technology, Delft,
    The Netherlands

Graphic abstract
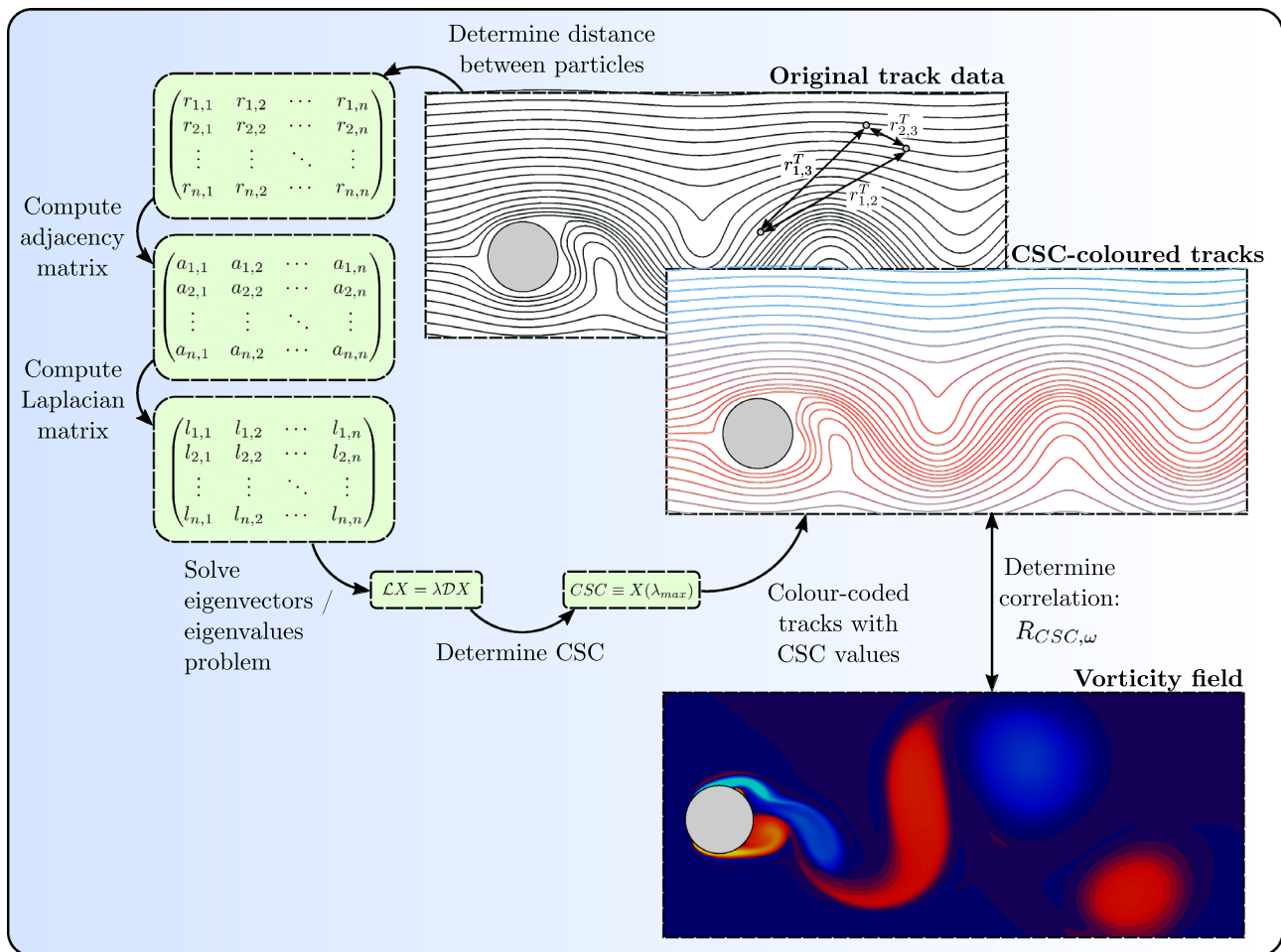
List of symbols

$\bar{r}_{ij}$ Mean distance between the i-th and j-th tracks

r_{ij} Instantaneous distance between the i-th and j-th tracks

$R_{x,y}$ Cross-correlation between x and y

λ Average inter-particle distance

L Track length

$\overline{V}$ Mean particle velocity

$|V|$ Mean flow velocity

D Characteristic length of the flow

ω Vorticity field

$\mathcal{A}$ Adjacency matrix

$\mathcal{L}$ Laplacian matrix

$\mathcal{D}$ Degree matrix

T Temporal track length

t flow time

a_{ij} Components of the second-order tensor $\mathcal{A}$

d_{ij} Components of the second-order tensor $\mathcal{D}$

X Eigenvector of the maximum eigenvalue ξ_{max}

ξ Eigenvalues of the spectral-clustering problem

x_i Components of the first-order tensor X

ψ Eulerian field

ϕ Function of formalized parameters

C Particle concentration, $[N/D^d]|d = 2, 3$

l Mean radius of large-scale structures

τ Mean characteristic period of large-scale structures, $\tau = l/V_T$

V_T Mean tangential velocity of large-scale structures

1 Introduction

Lagrangian particle tracking (LPT) is increasingly used due to its ability to quantity fluid-parcel trajectories in three-dimensional volumes. LPT is in principle suitable for the identification of Lagrangian coherent structures (LCS), i.e. repelling, attracting and shearing material surfaces can be extracted directly (Haller 2000; Haller and Yuan 2000). The identification of LCSs allows for a simplified assessment of a flow's topology, presenting a complete quantitation of material transport within an evolving fluid system (Haller 2015). In contrast, well-known Eulerian vortex detection methods are based on the decomposition of the velocity gradient tensor (Jeong and Hussain 1995), relying on the existence of relatively dense experimental data. Lagrangian methods are, however, not necessarily constrained by such requirements (Schlueter-Kuck and Dabiri 2017). This last feature drives the development of new post-processing strategies for the detection of coherent structures with data obtained from large-scale applications (Neamtu-Halic et al. 2019; Wei et al. 2019).

Lagrangian (trajectory-based) analysis allows for improved understanding of various processes that take place in the ocean, atmosphere and even in the lab, among other problems, which often suffer from poor spatial resolution (Mathur et al. 2019). In most of these cases, high spatial resolution is either impractical or impossible (Schmale and Ross 2015), resulting in incomplete and unreliable diagnostic fields. Resulting low signal-to-noise ratios motivate the development of alternative approaches that allow for accurate feature-detection in sparse data. Some of these studies concerning alternative approaches propose an Eulerian framework based on data assimilation (DA) (Ghil and Malanotte-Rizzoli 1991; Rodell et al. 2004), relying on the mix between numerical models and experimental data to create hybrid fields that generally have reduced uncertainty when compared to the original data sets. DA has been extensively adopted in weather forecasting, and has proved to be successful in detecting flow features in many complex system such as the ocean-atmosphere coupling model (Schiller et al. 1997) and the Arctic polar-vortex phenomenon (Swinbank and O'Neill 1994). Other examples where underlying flow dynamics have been revealed include oceanic, geophysical and atmospheric phenomena; see (Rodell et al. 2004; Cummings 2005; Bocquet et al. 2010). Notwithstanding, due to the necessity of a physical model, DA may not yet be possible for a variety of complex engineering, environmental and biological problems, e.g., the transport of pathogens in atmospheric flows (Schmale and Ross 2015) or the advection of micro organisms (Tallapragada et al. 2011). In such cases, the existence of a physical model is limited and the scales of the flows, up to thousands of kilometres, would make the task of detecting LCSs using DA challenging if not impossible.

Currently, flow structures from LPT data are typically identified using an Eulerian framework, by mapping the sparse LPT data onto a Cartesian grid, either through interpolation (Stüer and Blaser 2000) or by enforcing compliance with physical laws, e.g., by reconstructing scattered data using B-spline curves (Gesemann et al. 2016) or by interpolating particle track measurements using vortex models (Schneiders et al. 2017). Eulerian coherent structures are generally detected using diagnostic fields derived from the velocity gradient tensor. In such cases, cores of the vortical structures are defined as the connected regions in the flow where the velocity gradient tensor satisfies the product of the entries on its secondary diagonal being negative and smaller the product of the elements on the main diagonal (see (Chen et al. 2015)). Classical examples of Eulerian methods include the Q-, λ_2- and ω-fields (Zhan et al. 2019), all of those requiring that the velocity field exhibits a swirling pattern (Robinson 1991). But even though Eulerian techniques have been extensively adopted for the diagnostics and quantification of material surfaces, dense data sets are necessary for accurate estimation of the velocity gradient tensor (Green et al. 2007). Eulerian approaches also suffer from three major drawbacks: they are highly-sensitive to user-defined thresholds, the flow history is not taken into account in individual measurements (Rosi et al. 2015; Haller 2015), and observations conducted using Eulerian techniques change for non-inertial coordinate transformations (Jeong and Hussain 1995). Lagrangian descriptions of flow fields, on the other hand, allow for the observation of time-evolving flow features, and diagnostics are independent of the reference frame (Peacock and Dabiri 2010). Figure 1 illustrates typical results obtained from Eulerian and Lagrangian approaches with both densely and sparsely reconstructed flow fields for the canonical flow behind a square cylinder. Although widely adopted, classical Eulerian detection mechanisms are highly sensitive to vector spacing, and can result in large errors due to the larger-scale grid spacing of readily available atmospheric model data or the lack of high-resolution measurements in biological problems (e.g. (Sutton et al. 1994)).

It is also important to highlight the fact that traditional Lagrangian analyses, in which a velocity field is needed, are also not readily appropriate at large spatio-temporal scales. Some examples include the application of the classical finite-time Lyapunov exponent, FTLE (Haller 2001) and the finite-size Lyapunov exponent, FSLE (Boffetta et al. 2001). FTLE-fields have been extensively investigated in the past years to locate dynamical regions in geophysical flows (Peacock and Haller 2013; Pierrehumbert 1991; Toit
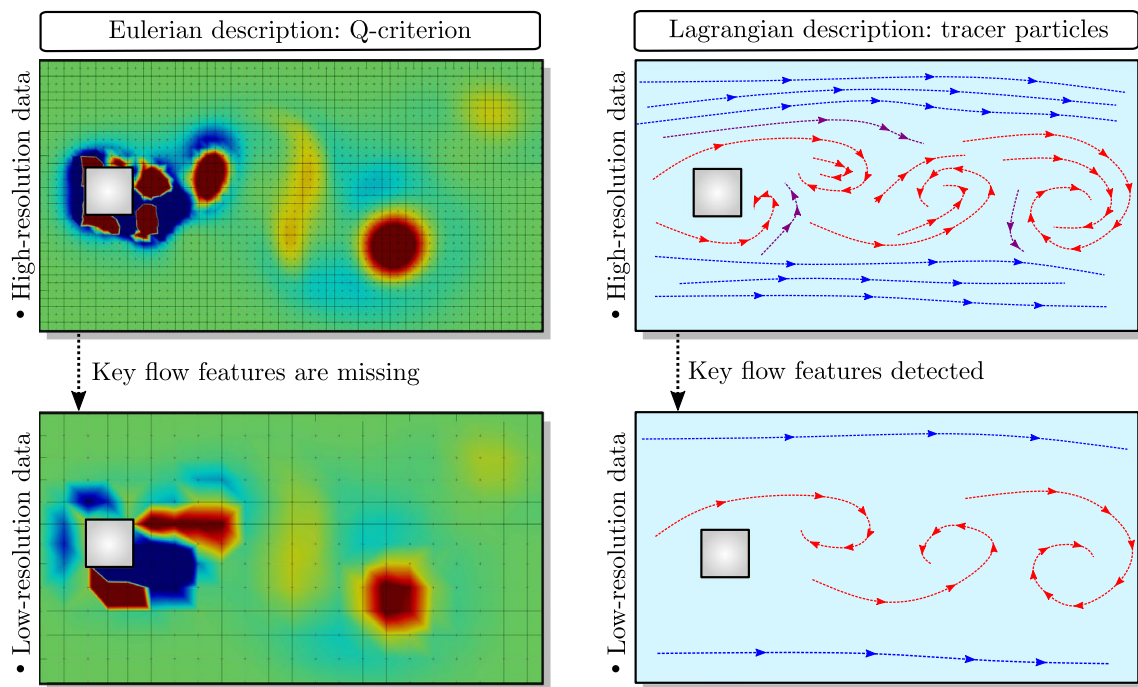
Fig. 1 (left) Eulerian and (right) Lagrangian descriptions of the flow behind a square cylinder. Q-criterion fields show vortical structures defined as convex topologies of $Q > 0$ (in red). In the top row, results obtained with a fine grid are shown. In the bottom row, the same results are extracted with a coarser grid spacing. In the latter, key flow features are not detected using the Eulerian description. In the Lagrangian description, the quality of the results is not necessarily constrained by the number of data points, allowing for the extraction of key flow features even with very sparse data.

2010), and for the detection of transport barriers in canonical flows (Kasten et al. 2010; Brunton and Rowley 2010). Nonetheless, despite the number of successful applications of the FTLE approach, the use of chaos-theory-based techniques for material-coherence detection presents several limitations, such as the fact that a discrete version of the flow field is naturally required. Furthermore, the analysis of the gradient tensor requires tracer trajectories to be sufficiently close so that necessary linearizations of the local velocity field's gradients remain accurate (Chu et al. 2003; Schlueter-Kuck and Dabiri 2017a). Owning to the obstacles of classical approaches for LCS-detection based on sparse data sets, new techniques that do not rely on the existence of dense data have recently been explored. Some of these approaches have been analysed by Hadjighasem et al. (2017) and motivate the current study.

Among these recently-developed approaches, the most promising technique for large-scale applications is the Coherent-Structure Colouring (CSC) algorithm proposed by Schlueter-Kuck and Dabiri (2017a), and applied in the present study. The CSC belongs to a category of Lagrangian methods that are based on spectral graph theory, originally proposed by Bezdek et al. (1984). The algorithm compares the spatial-evolution of an arbitrary number of tracer particles where tracks are colour-coded based on their dissimilarities. In practice, particle trajectories that present relatively small spatial deviation from each other are coloured with similar CSC values. Additionally, from a mathematical point-of-view, the kinematic dissimilarity between a pair of particles is not based upon the definition of a global coordinate system, making the CSC approach Lagrangian invariant (Haller 2015). Moreover, clustering techniques are not necessarily constrained by a minimum number of data points, meaning that the technique can still operate with indefinitely sparse data sets (Luxburg et al. 2008). Typical results obtained with the CSC approach are exemplified on the right-hand side of Fig. 1.

The convergence of coherent structures detected with CSC for an increasing number of tracer particles is to be expected, and has been verified by Schlueter-Kuck and Dabiri (2017b) in both two-dimensional flows and for synthetic data (see also Husic et al. (2019)). However, results obtained in these studies do not represent realistic data from large-scale, three-dimensional measurements. The ability to detect LCSs using CSC has only been tested with a relatively high concentration of synthetic tracer particles, precluding the findings of the original papers (Schlueter-Kuck and Dabiri 2017a, 2017b) to be extrapolated to real or complex atmospheric, oceanic or biological applications. Other questions still remain: for a realistic, three-dimensional flow,

what is the minimum recommended particle concentration that would still allow for coherent structure identification in CSC? What is the impact of track length on the overall quality of feature extraction? How does the CSC approach compare to classical Eulerian coherent-structure identification? What are important flow parameters to guarantee consistent results when using the CSC algorithm? In this paper, we address these above questions by using Shake-The-Box data from two benchmark flows: the flow-past the Ahmed body and a swirling jet flow. Tracks colour-coded using CSC will be compared to the baseline vorticity field, and the cross-correlation between features detected with both diagnostics are calculated and plotted versus flow parameters defined in the subsequent sections.

The current paper is organized as follows: In Sect. 2 we briefly introduce the mathematical background and notation for the implementation of CSC, and describe the adopted key normalized parameters. In Sect. 3, the experimental set-ups for two benchmark flows are presented. In Sect. 4, the correlation analysis between CSC and the baseline vorticity field are revealed. Lastly, conditions and limitations for the use of the technique with three-dimensional Lagrangian data are established (Fig. 2).

2 Methods

The following section is organized such that in Sect. 2.1 the mathematical description of the CSC method and the adopted notation are presented succinctly. In Sect. 2.2, normalized parameters for the investigation of the CSC method in realistic flows are developed and discussed.

2.1 Mathematical formulation

This section summarizes the CSC algorithm as recently explored by Schlueter-Kuck and Dabiri (2017a). The approach relies on the concept of a graph, a mathematical structure that consists of a set of nodes that are interconnected by edges. Nodes generally represent entities, while the edges describe the relationship between these entities, by both informing rather a pair of nodes is connected or not and what is the weight of that connection. In the CSC framework, the adopted graph is defined such that its nodes represent the measured Lagrangian particles, whilst edges represent the relationship between pairs of particles, being weighted by the kinematic dissimilarity of the respective tracers' trajectories. Such kinematic dissimilarity is defined as the standard deviation of the distance between two tracer particles during the measurement time, $t = (T - 1)\Delta t$, where T and Δt represent the temporal track length (number of samples within a track) and the measurement's time step, respectively.

Considering that N fluid particles with temporal track length of T are known, the weighted adjacency matrix $\mathcal{A}$ can be defined as:

$$a_{ij} = \frac{1}{\bar{r}_{ij} T^{1/2}} \left[\sum_{k=0}^{T-1} \left(\bar{r}_{ij} - r_{ij}(t_k) \right)^2 \right]^{1/2}, \tag{1}$$

which contains the weight of the edge that connects the i-th to the j-th particle. In Eq. 1, $\bar{r}_{ij}$ is the average distance between the two particles during the measurement time, whereas $r_{ij}(t_k)$ represents their instantaneous distance at the k-th time-step. The parameter a_{ij} is larger for particles that are kinematically dissimilar, whereas it is zero for particles
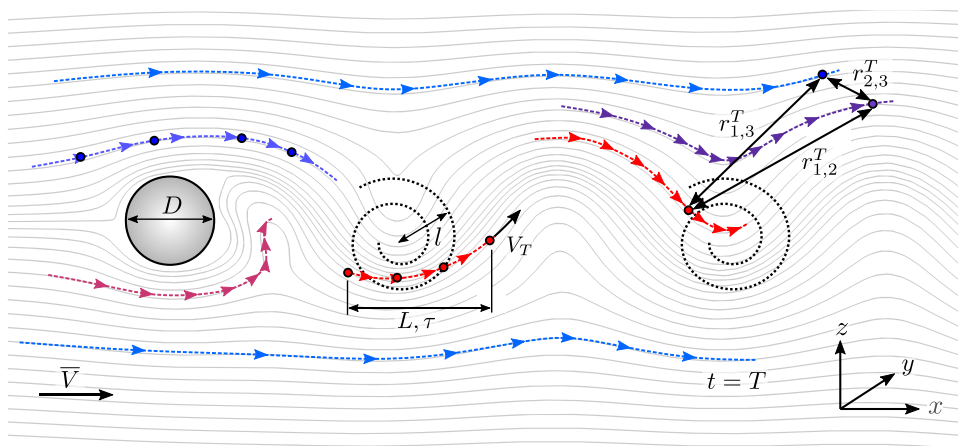

Fig. 2 Schematic of fluid domain with key normalized parameters. Fluid travelling at a mean velocity $\overline{V}$ interacts with an obstacle of characteristic length D, resulting in a circulation region with structures of radius l and a potential (surrounding) flow. Tracer particles in different flow domains will move with dissimilar kinematic responses, thus being colour-coded accordingly. All tracks possess a temporal track length of T, but tracks braided in between the large coherent eddies inherit a mean tangential velocity V_T and characteristic period τ. Track lengths L are related to the characteristic length of the flow and to the local flow velocity, such that $L \sim l \sim D$.

that keep their distance constant over time. For instance, if a pair of particles (i, j) move along straight parallel trajectories at the same velocity, then $a_{ij} = 0$. Contrarily, if the i-th particle moves along a straight trajectory whereas the j-th moves along a curvilinear one, then $a_{ij} > 0$.

Moreover, the degree matrix of a graph, $\mathcal{D}$, defined as:

$$d_{ij} = \begin{cases} 0, & \text{if } i \neq j \\ \sum_{k=1}^{N} a_{ik}, & \text{if } i = j, \end{cases} \tag{2}$$

contains with the k-th diagonal element the sum of the k-th row of the adjacency matrix $\mathcal{A}$. Defining now the graph Laplacian as $\mathcal{L} = \mathcal{D} - \mathcal{A}$, the graph colouring problem is such that node pairs with relatively large weights are associated with dissimilar values. This problem is equivalent to maximizing the expression:

$$z = \frac{1}{2} \sum_{i=1}^{N} \sum_{j=1}^{N} (x_i - x_j)^2 a_{ij} = X'\mathcal{L}X, \tag{3}$$

where X is a row vector containing the value of CSC of each particle, such that kinematically-dissimilar particles will be assigned largely varying z-values (Schlueter-Kuck and Dabiri 2017a). The problem of maximizing the expression in Eq. 3 is equivalent to that of finding the maximum eigenvalue ξ_{max} of the associated eigenvalues/eigenvectors system, $\mathcal{L}X = \xi\mathcal{D}X$, such that $X \equiv X(\xi_{max})$. The components of the eigenvector X associated with the maximum eigenvalue ξ_{max} represent the CSC of each particle. Particles with values of X similar in magnitude correspond to particles that are kinematically similar, and therefore that belong to the same Lagrangian coherent structure. The CSC is numerically implemented in MATLAB, and a synthetic pseudocode is given in the Appendix.

2.2 Normalized parameters

Considering a volume of fluid that scales with the characteristic length of the flow, D, and a homogeneous seeding distribution, it has been conjectured that accurate identification of LCSs is dependent on two key parameters: the track length L of the tracer particles; and the number N of particles present in the volume. The normalization of these parameters will be presented when considering a generic flow over a bluff body.

It is conjectured that the accuracy of the LCS identification based on the CSC method is dependent on the amount of the Lagrangian information in the flow field, relative to the size of the coherent structures. Hence, two relevant parameters are expected to play a role in the LCS identification: L/D and λ/D, where D is the characteristic length of the flow, L is the track length ($L = \overline{V}(T-1)$, being $\overline{V}$ the particle mean velocity along the track), and $\lambda = [3/(4\pi C)]^{1/3}$

is the average inter-particle distance, being C the tracers concentration. In general, L varies in space and time due to the flow non-uniformity. However, in the following analysis, the average value of L is considered. Also, a uniform seeding concentration is assumed, so that local and average inter-particle distances approximately coincide. From this analysis, the correlation between the results obtained with the CSC approach, and a reference Eulerian field ψ, are a function of the following Π-groups:

$$R_{CSC,\psi} = \phi(\Pi_1, \Pi_2) = \phi\left(\frac{\lambda}{D}, \frac{L}{D}\right), \tag{4}$$

where Π_1 and Π_1 refer to the normalized inter-particle distance and normalized mean track length, respectively.

The accuracy of the the CSC-based LCS identification is assessed by comparing the CSC with a standard Eulerian approach for vortex identification, namely the vorticity field. From preliminary results, it was concluded that the CSC approach holds strong correlation with the absolute-velocity and vorticity fields, but weak to null correlation with the Q or λ_2 criteria. The reasons for that will be further discussed in the the Results section of this work.

3 Experimental set-up and test cases

The first benchmark performed in this study is based on the flow behind a reference Ahmed body. Originally developed to investigate the features of flows around ground vehicles (Ahmed 1983), this simplified car model comprises a rounded fore-body, a box-like middle section and a slanted surface (slant angle of 25°) at the rear with rounded edges. The near-wake flow structure comprises two recirculation regions, and two longitudinal C-pillar vortices. The C-pillar-like structures are the most dominant characteristic material surfaces present in the near-wake region of the flow behind the Ahmed body, and are generated by the pressure difference between the flow coming from the vertical (lateral) walls of the model and the flow over the slanted surface (Ahmed et al. 1984). The flow behind the Ahmed body is presented in Fig. 3.

Data for the flow behind the Ahmed body was collected in the Open Jet Facility (OJF) of the TU Delft Aerodynamics Laboratories. The facility consists of a closed-loop, open test section wind tunnel with octagonal exit-section. The Ahmed body model is a 1 : 2 replica of the reference geometry, with slant angle of 25°, and rounded edges at the front face with radius of 50mm. The dimensions of the test model measure $522 \times 194.5 \times 144mm^3$. The reference, free-stream velocity was set to 12m/s, leading to a Reynolds number based on the model height, $H = 144mm$, of $Re = 1.15 \times 10^5$. The flow is seeded with neutrally buoyant helium-filled soap bubbles, with a seeding concentration
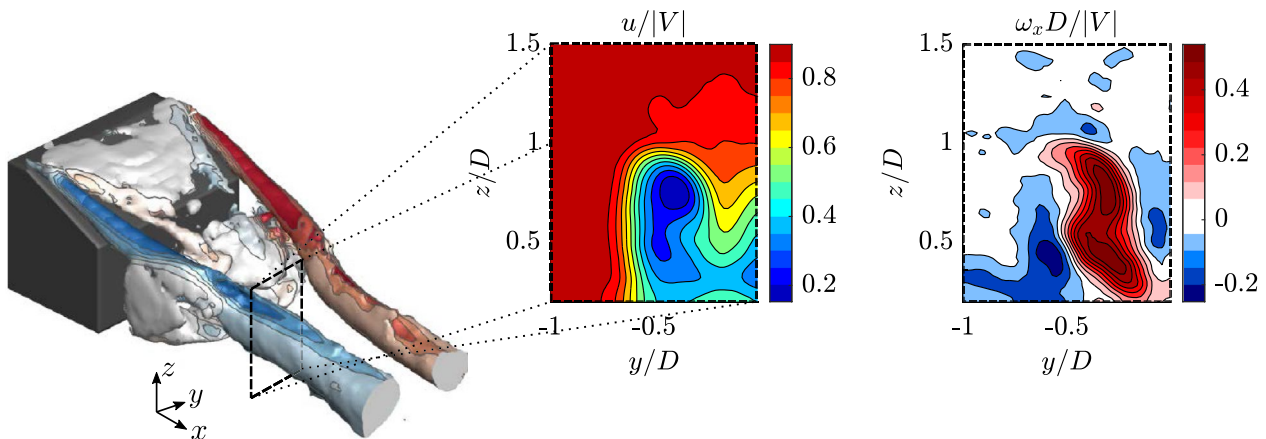
Fig. 3 (left) Time-averaged velocity distribution for the flow past the Ahmed body. Iso-contours of the Q-criterion ($Q = 4000s^{-2}$) coloured by the streamwise vorticity, ω_x, highlight the two C-pillar vortices. (center) Normalized streamwise velocity field, $u/|V|$, interpolated onto the cross-flow plane $0.5D$ downstream of the rear wall, where D is the height of the Ahmed body. (right) Normalized cross-flow vorticity field, $\omega_x D/|V|$, at the same cross-section position. Reference fields calculated with $N \sim 6.2 \times 10^6$ tracks

estimated as 0.3 particles per cm^3, yielding $0.03ppp$. Data is collected using the LaVision MiniShaker S probe, consisting of four CMOS sensor cameras installed into a single body, with a tomographic aperture of $4.3°$. Lagrangian particle tracking via the Shake-The-Box algorithm is conducted with illumination provided by a Quantronix Darwin Duo Nd:YLF laser located at the center of the probe. Time-resolved data is obtained at 700Hz, in a measurement volume of up to 130L, covering from the front of the model to approximately $2.2D$ downstream of the rear face. More detailed information concerning the conducted measurements are presented in Sciacchitano and Giaquinta (2019).

The second data set consists of a swirling jet flow. Experiments were performed in the Jet Tomographic Facility at the Aerodynamics Laboratories of TU Delft. The fluid domain consists of an octagonal water tank with diameter of 600mm, and a height of 800mm. Time-resolved data was collected in this volume of fluid at 100Hz, with a seeding density equal to approximately 300 particles per cm^3. The swirling jets emanate from nozzles of diameter 19.7mm, and have an average exit velocity of 0.05m/s, leading to a Reynolds number of $Re = 1000$. Results investigated in the present work are based on a flow with swirl number of $S = 0.2$. Lagrangian Particle Tracking via the Shake-The-Box algorithm is performed in LaVision DaVis 10. Other characteristics of the experimental measurement system are further discussed by Ianiro et al. (2018). The swirling jet flow was chosen as a benchmark for the CSC approach primarily because of its simple flow topologies and stationary behaviour, containing a long-lasting four-lobed-jet core.

4 Results and discussion

In the following, the performance of the CSC scheme is assessed on three-dimensional data based on comparison with the baseline vorticity field, ω. Tracks coloured using the CSC are interpolated onto a two-dimensional Cartesian grid, and the performance of the approach is calculated on a cell-by-cell fashion. The reference flow fields are shown in Figs. 3 and 4 for comparison. For each test case, unique set of parameters $\phi = \phi(\lambda/D, L/D)$ was indirectly selected by filtering from the data sets N particles with temporal track lengths of T. In this study, N ranged from 50 to 30000 tracks for both benchmarks, while T ranged from 4 to $0.9T_{max}$ time steps, where T_{max} represents the maximum temporal track length present in the respective data set. For the flow past the Ahmed body, these ranges of T and N are equivalent to inter-particle distance values of $\lambda/D \in [0.02, 0.4]$ and normalized track lengths of $L/D \in [0.1, 1.6]$. For the swirling jet flow, the parameter space consists of $\lambda/D \in [0.015, 0.18]$ and $L/D \in [0.02, 0.18]$. It is also important to emphasize that particle tracks in this study were randomly selected, which does not guarantee homogeneous seeding distribution, leading to broaden uncertainty in the estimation of the mean λ/D value. This issue has been addressed by computing high number of test cases for both benchmark flows.

Solutions of the CSC approach for the two benchmark flows were computed and resultant CSC-coloured tracks are illustrated in Fig. 5. Figure 5(a) and (b) show perspective views of $N = 10000$ colour-coded tracks of the Ahmed body and swirling jet flows, respectively. In each test case, tracks are represented in their entire extension. In these plots, solutions of the CSC approach are re-scaled to the interval $CSC \in [-1, 1]$, in which -1 is represented in dark blue and
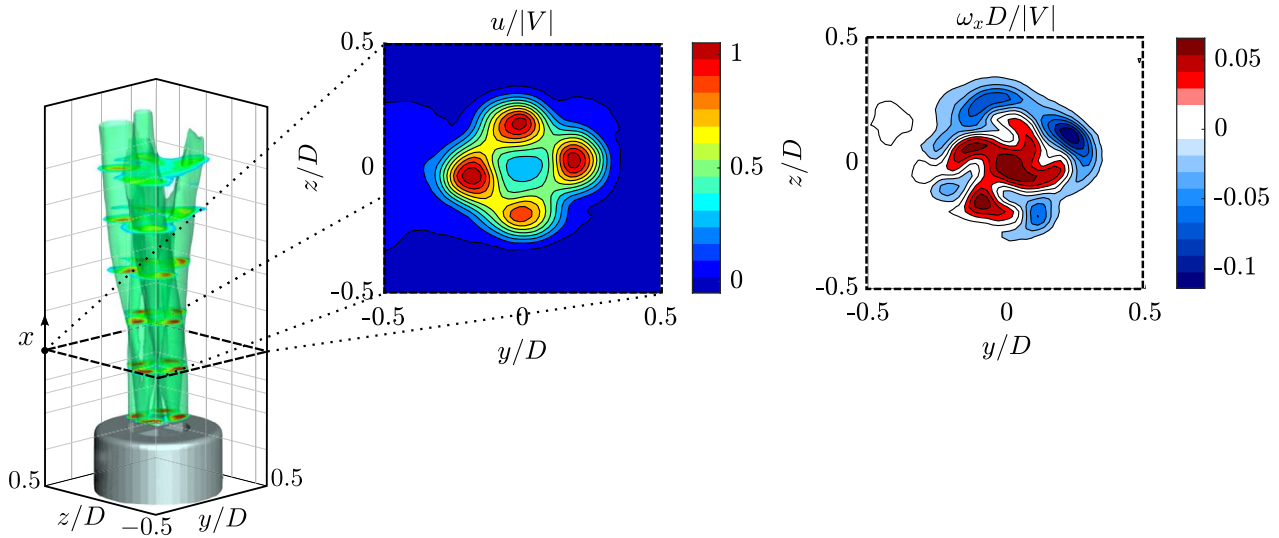
Fig. 4 (left) Time-averaged velocity distribution of the swirling-jet flow. Jet-cores are highlighted by the iso-contours of the absolute-velocity field at $V/|V| = 0.7$. (center) Normalized stream-wise velocity field, $u/|V|$, interpolated onto to the cross-flow plane $1D$ downstream of the nozzle-exits; and (right) Normalized cross-flow vorticity field, $\omega_x D/|V|$. Reference fields calculated with $N \sim 1 \times 10^6$ tracks.
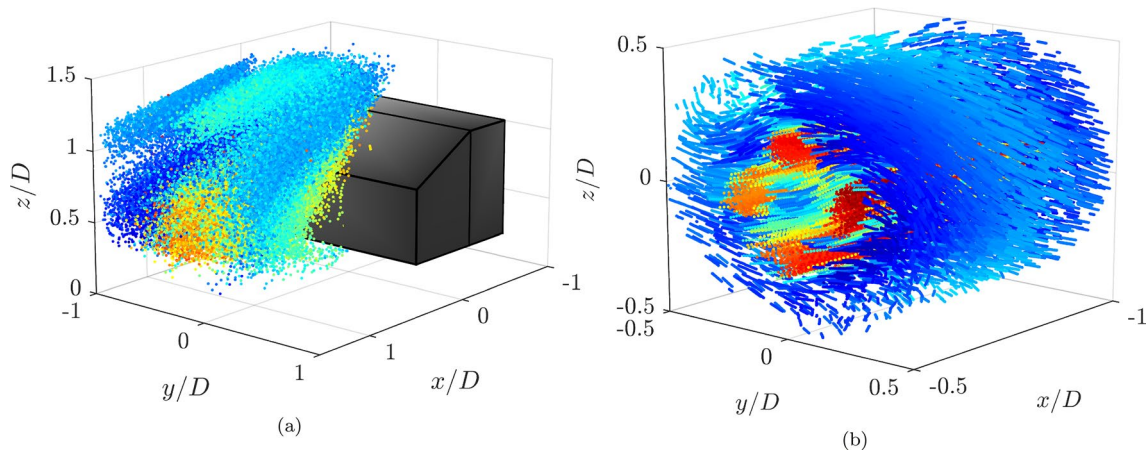

Fig. 5 (a) Perspective view of the flow past the Ahmed body for $\lambda/D \approx 0.06$ and $L/D \approx 0.8$, and (b) the swirling jet flow, with $\lambda/D \approx 0.05$ and $L/D \approx 0.14$. CSC values range from 1 (dark red) to -1 (dark blue) in the plots

1, in dark red, in the selected colour map. For the flow past the Ahmed body, for which results are shown in Fig. 5(a), there are clear evidences of successful detection of the left C-pillar vortex at the center of the tracers' trajectories. The core of the vortical structure is indicated by the tracks colour-coded in red. The C-pillar vortex is surrounded by green colour-coded tracks, representing the outer shear-layers of the coherent structure. Lastly, tracks laying inside the vortical material surface are surrounded by blue-coloured tracks, representing the transition to the potential-like flow. The test case shown in Fig. 5(a) contains instantaneous 10000 tracer particles with temporal track lengths of $T = 5$ time

steps (equivalent to $\lambda/D \approx 0.06$ and $L/D \approx 0.8$), and only the left-hand side portion of the flow-field is represented, for clarity. In Fig. 5(b), results for the swirling jet flow are shown for a test case with $N = 10000$ particles of temporal track length of $T = 30$ time steps (equivalent to $\lambda/D \approx 0.05$ and $L/D \approx 0.14$). As for the flow past the Ahmed body, the coherent features of the swirling jet flow are also easily identifiable in the CSC-coloured field. The four-lobed jet stream at the center of the fluid domain is colour-coded in red. A narrow transition region, representing the material surface in between the four lobes and the surrounding potential flow, is highlighted in green. The coherent jet stream is surrounded

by tracks coloured in blue, identifying the quiescent flow. Moreover, due to the considerably high particle concentration of the selected test case, the rain-drop-like shape of the convex lobes becomes evident in the CSC-coloured tracks.

4.1 Effects of the normalized parameters

CSC-coloured tracks of the flow past the Ahmed body and the swirling jet flow are shown in Figs. 6 and 7, respectively. Each figure illustrates the projection onto the cross-flow plane of the instantaneous CSC values, with each particle being represented by a single point at the instant $t = (T - 1)\Delta t / 2$. The top row shows the streamwise vorticity component obtained with the λ/D value of the respective column, for comparison. The first benchmark investigated in this work is the flow past the Ahmed body. The two longitudinal coherent eddies are the dominant structures of the flow and their cores travel further downstream symmetrically relatively to the xz-plane. For that reason, only the left-hand side portion of the fluid volume is analysed in this study, similarly to what is illustrated in the same figure. The two C-pillar vortexes are also relatively stationary (Sciacchitano and Giaquinta 2019), being this the reasons for selecting this flow as the first benchmark of the present study. This aspect is crucial for the analysis of this flow field since all tracks in the time interval are analysed simultaneously (i.e., as if the flow was stationary).

Here we examine two-parameters cases, for $L/D \approx [0.4, 1.0, 1.5]$ and $\lambda/D \approx [0.04, 0.09, 0.13]$. Figure 6 includes examples of baseline vorticity fields and CSC-coloured tracks obtained in the analysis. Columns, left to right, show results for decreasing λ/D values (increasing particle concentration). Rows, top to bottom, show results for increasing L/D values. In Figs. 6(a) to 6(c), vorticity fields obtained with $\lambda/D \approx 0.04, 0.09, 0.13$ are shown for comparison (note that the reference velocity and vorticity fields are shown in Fig. 4). For increasing L/D values, barely any difference is noticed in the colouring pattern of the tracer particles. This result is most likely associated with the fact that the relatively parallel streamlines do not allow for considerable increments of the kinematic dissimilarity as the flow moves further downstream. Based on the mathematical description of the CSC algorithm, it is evident that the method benefits from strong divergence in the tracers' trajectories, which is not sufficiently dominant in the data from flow past the Ahmed body. Another interesting remark is the fact that vortex detection is observed to work reasonably well independently of seeding gaps: the sparse seeding region centred at $(y/D, z/D) \approx (1, -0.5)$ did not prevent the algorithm from correctly distinguishing between particles (at the vicinity of the vortex's boundary) that belong to the vortex core from those at the potential-like flow. Non-uniform particle seeding is a common weakness among classical

clustering techniques that rely on absolute particle positions (Bezdek et al. 1984) since tracers from distant regions of the flow would be mistakenly clustered together by the adjacency matrix due to the absence of tracks in between them.

In the second benchmark, the swirling jet flow, the flow features a four-sectors-jet divided by the shear-layers resulting from the interactions along the vane walls. The four jet cores rapidly develop a quasi-homogeneous inner momentum distribution after the exit, featuring separation of their respective cores for increasing azimuthal distance due to the swirl number. In all test cases, the CSC approach was able to detect the existence of the four-lobed jet with some degree of accuracy, as it is shown in Fig. 7. Better feature-extraction performance occurs for decreasing inter-particle distance values, while the benefits of longer normalized track lengths are hardly noticeable, agreeing with the findings of Schlueter-Kuck and Dabiri (2017). It is also important to highlight the fact that the CSC algorithm assigns arbitrarily large or small values to the coherent structures. For this reason, colour inversions e.g., between panels 7(k) and 7(l) , occur. Alternatively, since the magnitude of the CSC values have no physical meaning, one could artificially change the resultant colour-mapping by computing $1 - CSC$ so that LCSs are always coloured with the same side of the colour spectrum.

Results in the left-most column of Fig. 7 represent flows with sparse particle seeding, resulting in $\lambda/D \approx 0.09$. At this condition, the spatial particle density is sufficient to observe the existence of the vortices, which can be distinguished by the region of red-coloured particles, but the outer shear-layers of the jets are still hardly noticeable. At $\lambda/D \approx 0.05$, at the center column, higher particle concentration values start to allow for the detection of both the existence of the four lobes and the stagnation region in between them. For $\lambda/D \approx 0.02$, at the right-most column, boundaries of the jet core start to become well defined and the characteristic four-lobed jet is easily identifiable in the Lagrangian data. Moreover, Figs. 7(d) and 7(a) represent a case in which the CSC method outperformed the baseline Eulerian diagnostic field. While the sparse CSC-coloured tracks shown in Fig. 7(d) already exhibit evidences of the existence of four lobes, with a small blue-coloured region separating them, the equivalent vorticity field, shown in Fig. 7(a), presents only a single macro structure that surrounds the four cores. This effect is directly associated with the fact that the sparsely interpolated vorticity field filters small discontinuities out from the interpolated velocity field, i.e., it "ignores" the three or four tracks with different velocity magnitude at the center of the jet stream. Such sequelae is not observed in a track colouring approach.

Effects of the track lengths are somewhat more ambiguous in comparison to those of the inter-particle distance. Comparing the results from $L/D \approx 0.015$ to $L/D \approx 0.15$ (top
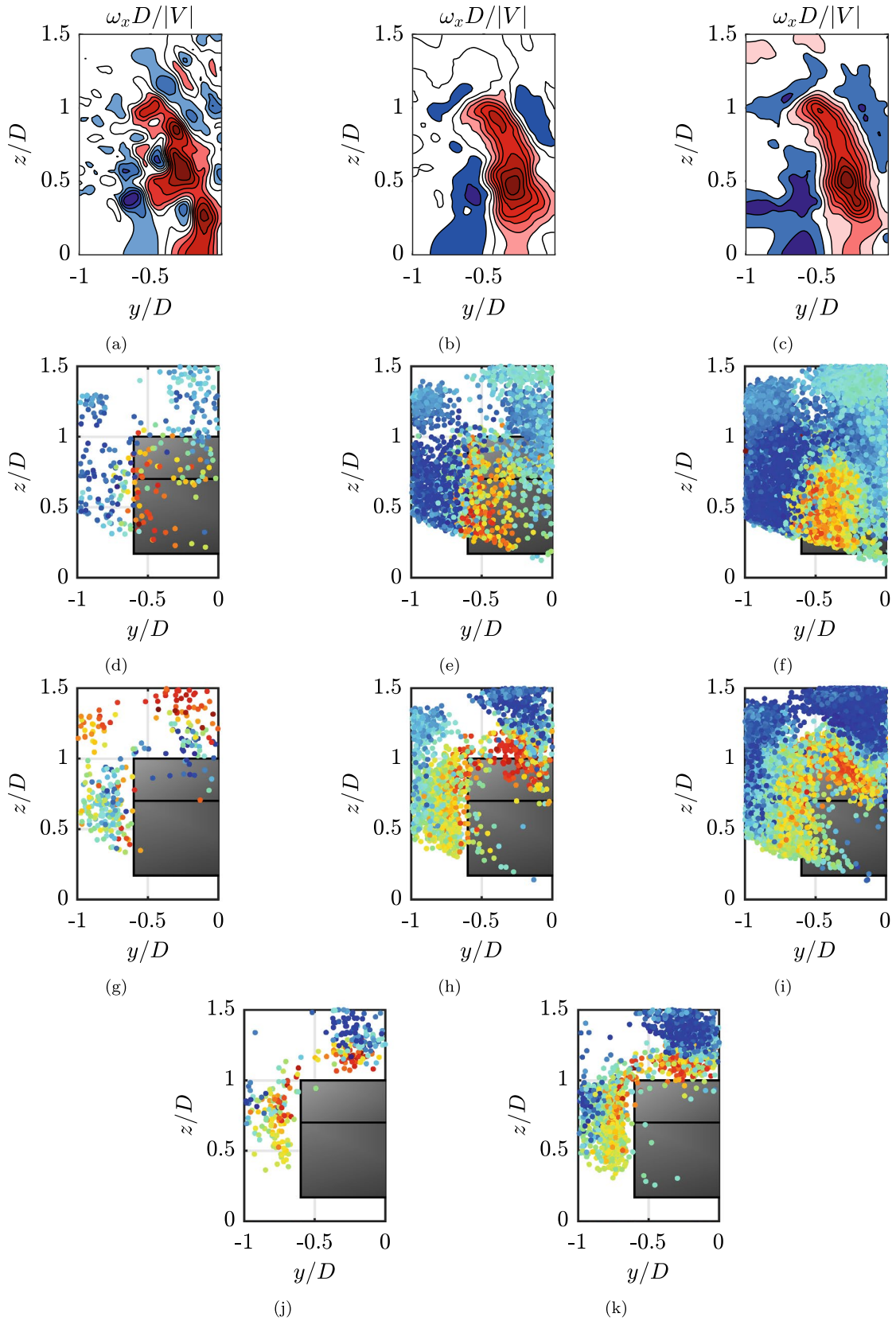
(a)   (b)   (c)

(d)   (e)   (f)

(g)   (h)   (i)

(j)   (k)

◄**Fig. 6** CSC-coloured tracks for the flow past the Ahmed body projected onto the cross-flow plane for $x/D \in [0.5, 1.0]$. Rows, top to bottom, show results for $L/D \approx 0.4$, 1.0 and 1.6, respectively. Columns, left to right, show results for $\lambda/D \approx 0.04$, 0.09 and 0.13, respectively. CSC values range in $[-1, 1]$, where -1 corresponds to blue and 1, to red, in the selected colour map. Results indicated as cases (d), (e), ..., (k) in Figs. 8(a) and 9(a) . Last row includes only the two right-most columns because selected L/D value would not allow achieving target density magnitude for the third column to be plot. Figures (a) to (c) show vorticity fields obtained with the corresponding λ/D values

to bottom rows of Fig. 7), no noticeable improvement in the identification of the Lagrangian coherent structures can be appreciated, even if the tracks length increases by one order of magnitude. Hence, it is concluded that the CSC results are mainly dependent on the inter-particle density, and therefore on the tracers concentration, whereas they are rather insensitive to the track length. Overall, for the CSC approach, it is more valuable to have more tracks of shorter length, rather than less longer tracks. This result belongs to the maxima that, as for any other clustering technique, more data points act as to converge the solution toward the "ground truth" (Luxburg et al. 2008). Results should also improve based upon the quality of the data, which, in the case of the CSC algorithm, is not directly dictated by the amount of Lagrangian information tracks carry (i.e., tracks lengths), but by how divergence tracks are. In that sense, the CSC approach depends on the number of tracer particles and on the flow characteristics, but not on the track lengths, as proposed in the second section of this work.

4.2 Correlation between the CSC and Eulerian diagnostics

The accuracy in detecting Lagrangian structures using the CSC approach was evaluated by computing the cross-correlation coefficient between CSC-field mapped onto a Cartesian grid and the streamwise vorticity component, ω_x, R_{CSC, ω_x}. Both the velocity and CSC-fields were interpolated into a Cartesian two-dimensional grid, projected onto the cross-flow plane. Flow parameters of each grid cell were computed using the average of the (u, v, w, CSC)-values of all particles that lay within it. The sparse velocity and CSC values are mapped onto a Cartesian bin by averaging their values within cubic bins of 0.02cm size, with 75% overlap, following the approach proposed by Aguera et al. (2016). The binning is conducted for varying values of the tracers concentration (viz. λ) and of the tracks length (L) to assess the effect of these two parameters onto the quality of the CSC results.

Figure 8 shows results of the CSC algorithm using increasing inter-particle distance values. For both flows, increasing inter-particle distance values leads to loss in

the accuracy of the method, as expected. Schlueter-Kuck and Dabiri (2017a) obtained similar results, emphasising also that the method is dependent on prior knowledge of the size of the vortical structures in order to secure appropriate sparsification levels. In their work, Schlueter-Kuck and Dabiri (2017a) concluded that numbers of particles in the order of hundreds, equivalent to $\mathcal{O}(\lambda/D) > 10^{-1}$ in the investigated flows, would be insufficient to accurately detect LCSs, agreeing with what is shown in Fig. 8. The trend of the results, on the other hand, is not monotonic. For the swirling jet flow, for example, there is a slight decrease in the overall cross-correlation values for low values of λ/D. This particular characteristic is most likely due to to the fact that the four-lobed convex jet stream goes from an ellipsoidal to a "raindrop-like" shape for $\lambda/D < 0.05$ when computed by the CSC (compare Figs. 7(e) and 7(f), for example). On the other hand, the vorticity or absolute-velocity fields tend to exhibit predominantly rounded-like jet-cores. Another remark observed in the same plots is the fact that the correlation function converges to a single value for decreasing values of λ/D independently of the track length. This characteristic allows for the technique to be considered spatially-convergent, part of the set of basic requirements that have proven necessary for self-consistent LCS results (Haller 2015).

Contrarily to what was observed for the normalized inter-particle distance, the cross-correlation function does not show any particular trend with varying normalized track lengths, as it is shown again in Fig. 9. Short track lengths will naturally lead to a less accurate estimation of the kinematic dissimilarities between track pairs, but the reciprocal is not necessarily true for increasing track lengths. The comparison of cases 7(e) and 7(h) (see also Fig. 7) proves that the increment of L/D value by 500% did not result into an appreciable improvement of the estimated cross-correlation coefficient. A similar conclusion can be drawn for the flow past the Ahmed body, for which results are shown in Fig. 9(a). Based on the results presented so far, it is concluded that the results of the CSC algorithm are independent of the tracks length, as long as the latter exceeds a certain minimum. Based on the current results, such minimum is estimated to about 1% of the flow characteristic length.

As a final remark, it is also important to highlight one of the biggest drawbacks of the current description of the CSC: the method works in a binary fashion, by detecting that a single ensemble of tracer particles behaves differently from all the rest, regardless of the real number of vortical structures shed in the flow. This characteristic can be illustrated by analysing the CSC-coloured tracks of the swirling jet flow: in all test cases, its characteristic four-lobed jet is colour-coded in a single colour (e.g, red), while the remaining particles in the quiescent flow are colour-coded in blue, for example. If all flow features were
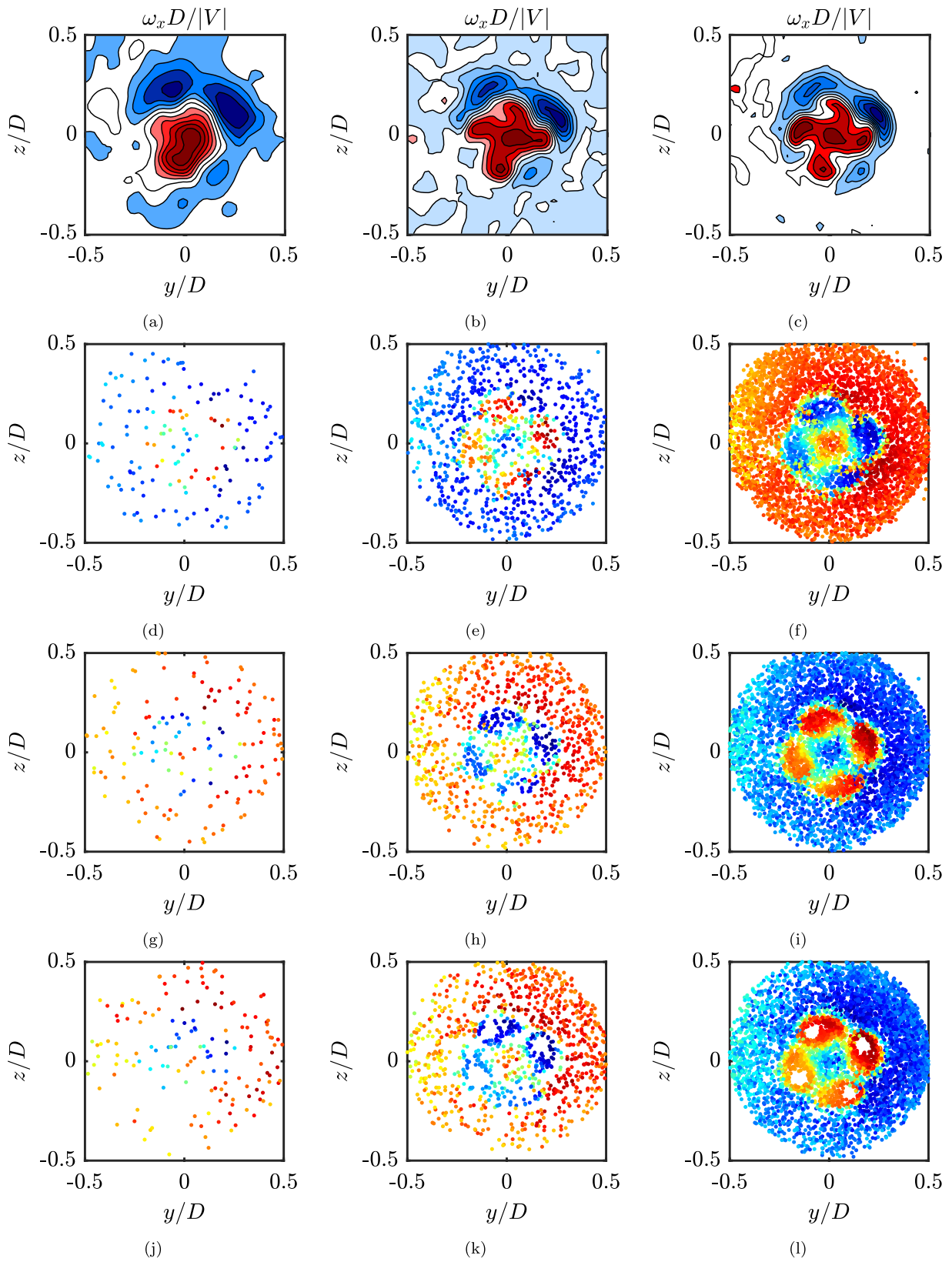
(a)   (b)   (c)

(d)   (e)   (f)

(g)   (h)   (i)

(j)   (k)   (l)

◄**Fig. 7** CSC-coloured tracks for the swirling-jet flow projected onto the cross-flow plane for $x/D \in [-1.0, -0.5]$. Rows, top to bottom, show results for constant L/D values of ≈ 0.015, 0.08 and 0.015, respectively. CSC values range in $[-1, 1]$, where -1 corresponds to blue and 1, to red, in the selected colour map. Columns, left to right, show results for λ/D values of ≈ 0.09, 0.05 and 0.02, respectively. Results obtained in cases (d), (e), ..., (l) are indicated in Figs. 8(b) and 9(b) . Figures (a) to (c) show vorticity fields obtained with the corresponding λ/D values

in nature to the definition of the absolute-velocity field. Both the Q and λ_2 criteria are, on the other hand, proper individual features detection mechanisms (Jeong and Hussain 1995), highlighting individual convex helical structures that rotate about the symmetry axis of the jet cores (see Dulin et al. (b)) and, therefore, are not strongly correlated to what the CSC-coloured tracks express.

individually detected by the CSC approach, as hoped-for, one would expect to see the four lobes of the swirling jet coloured with four dissimilar CSC-values. In that sense, the CSC approach distinguishes rotational zones from the potential-like ones, but it is not meant for individual features detection, per se.

This characteristic of the CSC approach is the key reason behind the fact that strong correlation is observed between the CSC-coloured tracks and the absolute-velocity field (up to 95% in the tests with the present benchmarks), but small correlation is obtained between the Lagrangian approach and the Q or λ_2 criteria (less than 20% with the present benchmarks), for example. In the swirling jet flow, the four lobes of the jet travel at a similar mean velocity that is considerably higher than that of the surrounding quiescent mean. The CSC approach detects the high congruence of the relative motion of particles inside the jet cores in comparison to the particles at the quiescent mean, and this result is very similar

5 Conclusions

In this study, three-dimensional coherent flow structures were detected using sparse track data for the first time using the Coherent-Structure Colouring (CSC) algorithm. Three-dimensional PTV data of the canonical flow past the Ahmed reference body and a swirling jet flow were adopted as benchmarks. The accuracy in the detection of coherent eddies was evaluated using the cross-correlation between the CSC-field with the baseline vorticity field, based on the two-dimensional projection onto the cross-flow plane of both diagnostic fields. It was concluded that higher accuracy in the coherent structures identification is obtained for decreasing inter-particle distance. Conversely, the CSC results were independent of track length, as long as the mean inter-particle distances did not exceed 15% of the characteristic length scale.
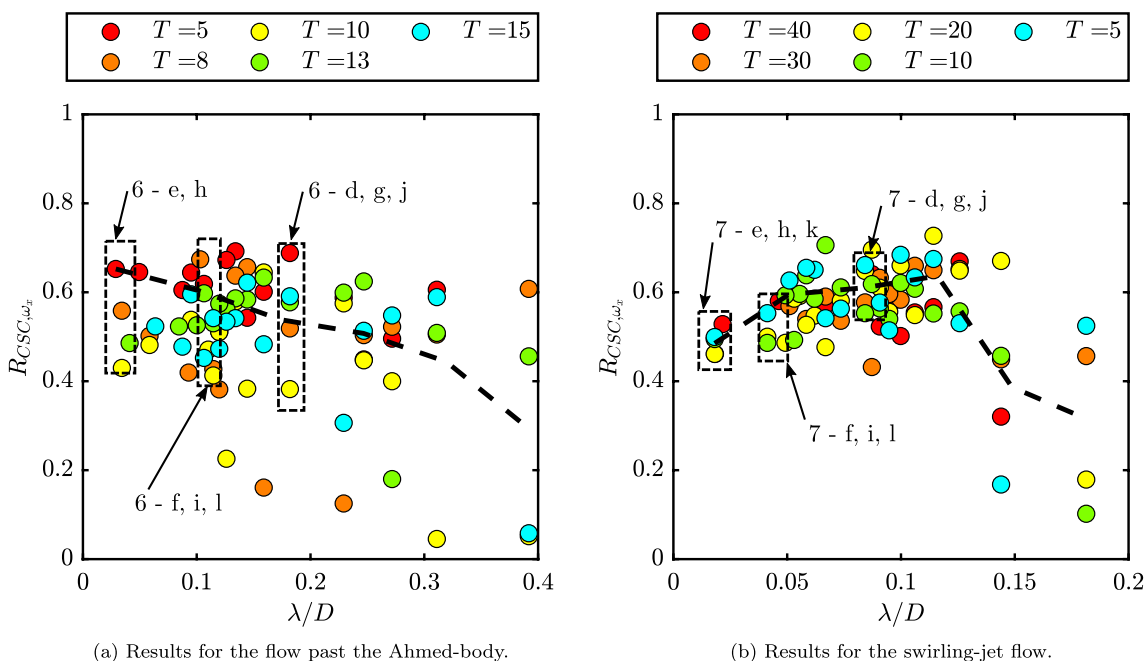

(a) Results for the flow past the Ahmed-body.

(b) Results for the swirling-jet flow.

Fig. 8 Cross-correlation function versus normalized inter-particle distance for (a) the flow past the Ahmed body; and the (b) swirling jet flow. Reference cases for the respective benchmarks are highlighted by the dashed lines and refer to results shown in Figs. 6 and 7 . Thick dashed lines indicate the trend of the data points
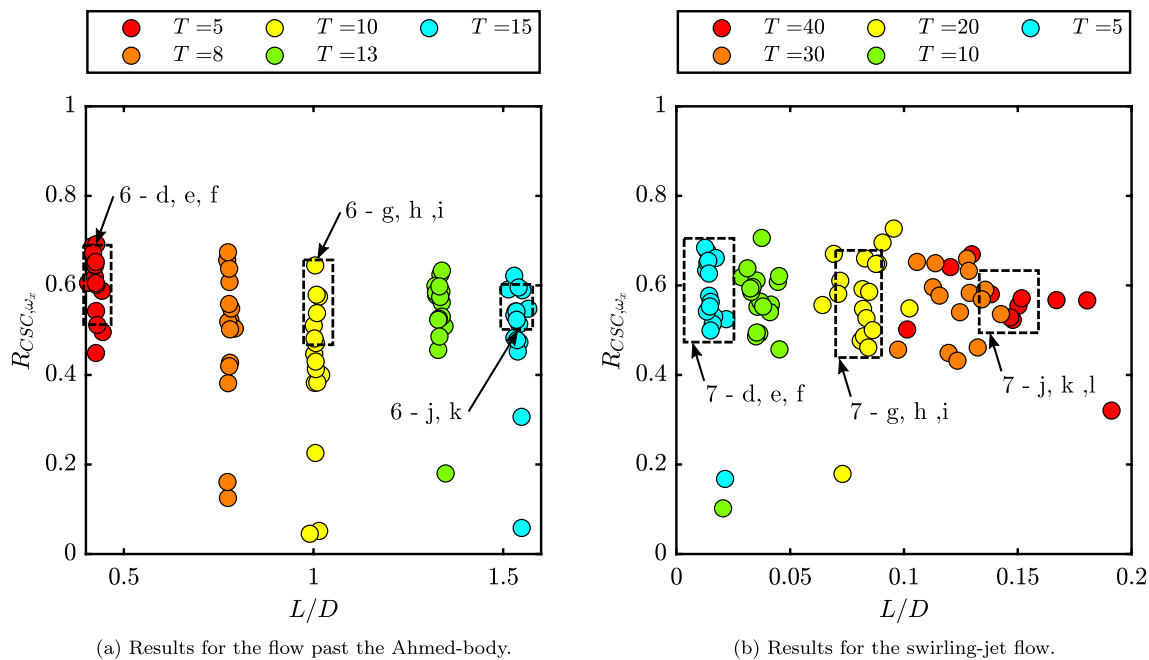
(a) Results for the flow past the Ahmed-body.

(b) Results for the swirling-jet flow.

Fig. 9 Cross-correlation function versus normalized track-length for (a) the flow past the Ahmed body; and the (b) swirling jet flow. Reference cases for the respective benchmarks are highlighted by the dashed lines and refer to results shown in Figs. 6 and 7 . Thick dashed lines indicate the trend of the data points

References

Agüera N, Cafiero G, Astarita T, Discetti S (2016) Ensemble 3d ptv for high resolution turbulent statistics. Measurement Science and Technology 27(12):124,011

Ahmed S (1983) Influence of base slant on the wake structure and drag of road vehicles. SAE Transactions

Ahmed SR, Ramm G, Faltin G (1984) Some salient features of the time-averaged ground vehicle wake. SAE Transactions pp 473–503

Bezdek JC, Ehrlich R, Full W (1984) Fcm: The fuzzy c-means clustering algorithm. Computers & Geosciences 10(2–3):191–203

Bocquet M, Pires CA, Wu L (2010) Beyond gaussian statistical modeling in geophysical data assimilation. Monthly Weather Review 138(8):2997–3023

Boffetta G, Lacorata G, Redaelli G, Vulpiani A (2001) Detecting barriers to transport: a review of different techniques. Physica D: Nonlinear Phenomena 159(1–2):58–70

Brunton SL, Rowley CW (2010) Fast computation of finite-time lyapunov exponent fields for unsteady flows. Chaos: An Interdisciplinary Journal of Nonlinear Science 20(1):017,503

Chen Q, Zhong Q, Qi M, Wang X (2015) Comparison of vortex identification criteria for planar velocity fields in wall turbulence. Physics of Fluids 27(8):085,101

Chu PC, Ivanov LM, Korzhova TP, Margolina TM, Melnichenko OV (2003) Analysis of sparse and noisy ocean current data using flow decomposition. part ii: Applications to eulerian and lagrangian data. Journal of Atmospheric and Oceanic Technology 20(4):492–512

Cummings JA (2005) Operational multivariate ocean data assimilation. Quarterly Journal of the Royal Meteorological Society: A journal of the atmospheric sciences, applied meteorology and physical oceanography 131(613):3583–3604

Du Toit PC (2010) Transport and separatrices in time-dependent flows. PhD thesis, California Institute of Technology

Dulin VM, Abdurakipov S, Markovich D, Hanjalic K (2017) Dynamics of large-scale vortices in non-swirling and swirling turbulent jets. time-resolved tomographic piv measurements. In: Proceedings of the 10th International Symposium on Turbulence and Shear Flow Phenomena, vol 3, p 233

Gesemann S, Huhn F, Schanz D, Schröder A (2016) From noisy particle tracks to velocity, acceleration and pressure fields using b-splines and penalties. In: 18th international symposium on applications of laser and imaging techniques to fluid mechanics, Lisbon, Portugal, pp 4–7

Ghil M, Malanotte-Rizzoli P (1991) Data assimilation in meteorology and oceanography. In: Advances in geophysics, vol 33, Elsevier, pp 141–266

Green MA, Rowley CW, Haller G (2007) Detection of lagrangian coherent structures in three-dimensional turbulence. Journal of Fluid Mechanics 572:111

Hadjighasem A, Farazmand M, Blazevski D, Froyland G, Haller G (2017) A critical comparison of lagrangian methods for coherent structure detection. Chaos: An Interdisciplinary Journal of Nonlinear Science 27(5):053,104

Haller G (2000) Finding finite-time invariant manifolds in two-dimensional velocity fields. Chaos: An Interdisciplinary Journal of Nonlinear Science 10(1):99–108

Haller G (2001) Distinguished material surfaces and coherent structures in three-dimensional fluid flows. Physica D: Nonlinear Phenomena 149(4):248–277

Haller G (2015) Lagrangian coherent structures. Annual Review of Fluid Mechanics 47:137–162

Haller G, Yuan G (2000) Lagrangian coherent structures and mixing in two-dimensional turbulence. Physica D: Nonlinear Phenomena 147(3–4):352–370

Husic BE, Schlueter-Kuck KL, Dabiri JO (2019) Simultaneous coherent structure coloring facilitates interpretable clustering of scientific data by amplifying dissimilarity. Plos one 14(3):e0212,442

Ianiro A, Lynch KP, Violato D, Cardone G, Scarano F (2018) Three-dimensional organization and dynamics of vortices in multichannel swirling jets. Journal of Fluid Mechanics 843:180–210

Jeong J, Hussain F (1995) On the identification of a vortex. Journal of fluid mechanics 285:69–94

Kasten J, Petz C, Hotz I, Hege HC, Noack BR, Tadmor G (2010) Lagrangian feature extraction of the cylinder wake. Physics of fluids 22(9):091,108

Mathur M, David MJ, Sharma R, Agarwal N (2019) Thermal fronts and attracting lagrangian coherent structures in the north bay of bengal during december 2015-march 2016. Deep Sea Research Part II: Topical Studies in Oceanography 168(104):636

Neamtu-Halic MM, Krug D, Haller G, Holzner M (2019) Lagrangian coherent structures and entrainment near the turbulent/non-turbulent interface of a gravity current. Journal of fluid mechanics 877:824–843

Peacock T, Dabiri J (2010) Introduction to focus issue: Lagrangian coherent structures

Peacock T, Haller G (2013) Lagrangian coherent structures: The hidden skeleton of fluid flows. Physics today 66(2):41–47

Pierrehumbert R (1991) Large-scale horizontal mixing in planetary atmospheres. Physics of Fluids A: Fluid Dynamics 3(5):1250–1260

Robinson SK (1991) Coherent motions in the turbulent boundary layer. Annual Review of Fluid Mechanics 23(1):601–639

Rodell M, Houser P, Jambor U, Gottschalck J, Mitchell K, Meng CJ, Arsenault K, Cosgrove B, Radakovich J, Bosilovich M et al (2004) The global land data assimilation system. Bulletin of the American Meteorological Society 85(3):381–394

Rosi GA, Walker AM, Rival DE (2015) Lagrangian coherent structure identification using a voronoi tessellation-based networking algorithm. Experiments in Fluids 56(10):189

Schiller A, Mikolajewicz U, Voss R (1997) The stability of the north atlantic thermohaline circulation in a coupled ocean-atmosphere general circulation model. Climate Dynamics 13(5):325–347

Schlueter-Kuck KL, Dabiri JO (2017a) Coherent structure colouring: identification of coherent structures from sparse data using graph theory. Journal of Fluid Mechanics 811:468–486

Schlueter-Kuck KL, Dabiri JO (2017) Identification of individual coherent sets associated with flow trajectories using coherent structure coloring. Chaos: An Interdisciplinary Journal of Nonlinear Science 27(9):091,101

Schmale III DG, Ross SD (2015) Highways in the sky: Scales of atmospheric transport of plant pathogens. Annual review of phytopathology 53

Schneiders JF, Scarano F, Elsinga GE (2017) Resolving vorticity and dissipation in a turbulent boundary layer by tomographic ptv and vic+. Experiments in Fluids 58(4):27

Sciacchitano A, Giaquinta D (2019) Investigation of the ahmed body cross-wind flow topology by robotic volumetric piv. In: Proceedings of the 13th International Symposium on Particle Image Velocimetry, Universitat der Bundeswehr Munchen

Stüer H, Blaser S (2000) Interpolation of scattered 3d ptv data to a regular grid. Flow, turbulence and combustion 64(3):215–232

Sutton RT, Maclean H, Swinbank R, O'Neill A, Taylor F (1994) High-resolution stratospheric tracer fields estimated from satellite observations using lagrangian trajectory calculations. Journal of the atmospheric sciences 51(20):2995–3005

Swinbank R, O'Neill A (1994) A stratosphere-troposphere data assimilation system. Monthly Weather Review 122(4):686–702

Tallapragada P, Ross SD, Schmale III DG (2011) Lagrangian coherent structures are associated with fluctuations in airborne microbial populations. Chaos: An Interdisciplinary Journal of Nonlinear Science 21(3):033,122

Von Luxburg U, Belkin M, Bousquet O (2008) Consistency of spectral clustering. The Annals of Statistics pp 555–586

Wei C, Tanner HG, Yu X, Hsieh MA (2019) Low-range interaction periodic rendezvous along lagrangian coherent structures. In: 2019 American Control Conference (ACC), IEEE, pp 4012–4017

Zhan Jm, Li Yt, Wai WhO, Hu Wq (2019) Comparison between the q criterion and rortex in the application of an in-stream structure. Physics of Fluids 31(12):121,701